Diffusionless isothermal omega transformation in titanium alloys driven by quenched-in compositional fluctuations

Masakazu Tane,[1,2,*] Hiroki Nishiyama,[1] Akihiro Umeda,[1] Norihiko L. Okamoto,[2] Koji Inoue,[2] Martin Luckabauer,[2] Yasuyoshi Nagai,[2] Tohru Sekino,[1] Takayoshi Nakano,[3] and Tetsu Ichitsubo[2]

[1]*Institute of Scientific and Industrial Research, Osaka University, Ibaraki, Osaka 567-0047, Japan*

[2]*Institute for Materials Research, Tohoku University, Sendai, Miyagi 980-8577, Japan*

[3]*Division of Materials and Manufacturing Science, Graduate School of Engineering, Osaka University, Suita, Osaka 565-0871, Japan*

(Received 22 January 2019; published 16 April 2019)

In titanium alloys, the ω(hexagonal)-phase transformation has been categorized as either a diffusion-mediated isothermal transformation or an athermal transformation that occurs spontaneously via a diffusionless mechanism. Here we report a diffusionless isothermal ω transformation that can occur even above the ω transformation temperature. In body-centered cubic β-titanium alloyed with β-stabilizing elements, there are locally unstable regions having fewer β-stabilizing elements owing to quenched-in compositional fluctuations that are inevitably present in thermal equilibrium. In these locally unstable regions, diffusionless isothermal ω transformation occurs even when the entire β region is stable on average so that athermal ω transformation cannot occur. This anomalous, localized transformation originates from the fluctuation-driven localized softening of $2/3[111]_\beta$ longitudinal phonon, which cannot be suppressed by the stabilization of β phase on average. In the diffusionless isothermal and athermal ω transformations, the transformation rate is dominated by two activation processes: a dynamical collapse of $\{111\}_\beta$ pairs, caused by the phonon softening, and a nucleation process. In the diffusionless isothermal transformation, the ω-phase nucleation, resulting from the localized phonon softening, requires relatively high activation energy owing to the coherent β/ω interface. Thus, the transformation occurs at slower rates than the athermal transformation, which occurs by the widely spread phonon softening. Consequently, the nucleation probability reflecting the β/ω interface energy is the rate-determining process in the diffusionless ω transformations.

DOI: 10.1103/PhysRevMaterials.3.043604

I. INTRODUCTION

Titanium alloys are indispensable for structural and biomedical materials because they exhibit high strength, corrosion resistance, and biocompatibility [1–3]. In particular, body-centered cubic β-Ti alloys have attracted interest owing to their superior functional and mechanical properties such as shape-memory effect, superelasticity, and low Young's modulus [3,4]. To control these superior properties, an in-depth understanding of phase transformations from the metastable β phase is of great importance. Recently, ω(hexagonal)-phase transformation from the β phase has attracted much attention, because it can be utilized for the formation of unique nanostructures composed of orthorhombic α'' martensite or hexagonal close-packed α phase within the β-matrix [5–7]. These findings constitute a paradigm shift in titanium science, as emphasis was traditionally placed on the prevention of formation of ω phase, owing to its negative impact on mechanical properties such as the increase in ductility and Young's modulus [8,9].

Owing to the importance of ω transformation, its formation mechanism has been studied extensively [8,10–13]. In β-Ti alloys, ω transformation occurs via a periodic collapse of $(111)_\beta$ lattice plain pairs, in response to a softening of the $2/3[111]_\beta$ longitudinal phonon mode [10] [see Supplemental Material, Fig. S1(a) [14]]. Importantly, in the ω transformation, the transformation strain (eigenstrain) is small, similar to the case of premartensite transformation, which occurs via a shuffling motion of atomic planes [15,16]. Therefore, the ω transformation is accompanied not by the softening of long wavelength acoustic phonon at the gamma point but by the softening of short wavelength acoustic phonon [17].

In terms of the transformation kinetics, the ω transformation has been categorized into two transformation modes [8,10]: athermal and isothermal ω transformations. At low temperatures, where atomic diffusion cannot occur, the ω transformation occurs instantaneously via a diffusionless mechanism; this is called *athermal ω transformation* [8]. In contrast, at temperatures above ~500 K, *isothermal ω transformation*, which exhibits an incubation time for transformation, occurs [8]. In this case, solute-atom partitioning occurs via atomic diffusion, and in the resultant solute lean β-phase regions, athermal ω transformation occurs. Consequently, the atomic diffusion is the origin of the observed incubation time in the isothermal ω transformation.

However, in some previous studies, researchers claimed that the ω phase is also formed during isothermal aging at room temperature (RT) [18–20] where atomic diffusion cannot occur. Recently, Tane *et al.* [21] revealed that a

*mtane@sanken.osaka-u.ac.jp

"diffuse ω structure" [8] is closely related to the isothermal ω transformation near RT. These reports indicate that a *diffusionless isothermal ω transformation* possibly occurs near RT. Consequently, the classification of ω transformations must be reconstructed. Furthermore, from a thermodynamic point of view, athermal ω transformation near the transformation temperature T_ω has not been understood yet. In less stable β-Ti alloys, a diffuse ω structure is formed above an athermal ω transformation temperature T_ω [10]. At T_ω, athermal ω transformation does not occur in the entire β matrix, and it gradually proceeds via cooling below T_ω [10], although $\beta \leftrightarrow \omega$ athermal transformation does not exhibit a temperature hysteresis, i.e., large undercooling is not required for the transformation. To clarify these unsolved problems and construct a universal ω transformation theory, we explore the detailed mechanism of the diffusionless isothermal and athermal ω transformations in the Ti-V alloy system.

II. METHODS

Master alloys with nominal compositions Ti-21V and Ti-27V (at.%), showing different ω transformation behaviors, were prepared from high-purity Ti and V via arc melting. In the Ti-21V alloy whose β-phase is less stable, the athermal ω transformation temperature T_ω is 230 K [22]. In the Ti-27 V alloy whose β-phase is more stable, the athermal ω transformation does not occur down to cryogenic temperatures [see Supplemental Material, Fig. S1(b) [14]]. Single crystals were grown from the master alloys using a floating-zone method at a crystal growth rate of 2.5 mm h^{-1} in Ar atmosphere. V concentrations in the prepared single crystals were analyzed using inductively coupled plasma atomic emission spectrometry, and the oxygen and nitrogen contents were determined using an oxygen-nitrogen analyzer. The analyzed compositions were Ti-20.72%V-0.42%O-0.08%N and Ti-27.91%V-0.33%O-0.06%N in at.% units.

Cubic specimens of $\sim 4 \times 4 \times 4$ mm^3 were cut from the single-crystal ingots for the measurements of elastic properties, resonance frequencies, and internal friction Q^{-1}. Furthermore, disk-shaped specimens of diameter $\sim$9 mm were cut from the single-crystal ingots for the XRD measurements. The cubic specimen surfaces were parallel to $\{100\}_\beta$ and the flat surfaces of disk-shaped specimens were parallel to $\{111\}_\beta$. These single-crystalline specimens were subjected to a solid-solution treatment at 1273 K for 1 h in vacuum and were subsequently quenched in iced water.

For the disk-shaped specimens after quenching, the XRD patterns near $(0002)_\omega$ and $(222)_\beta$ were measured during aging at $\sim$300 K for 10 days. The measurements were conducted in planes parallel to $(222)_\beta$ using CuKα radiation. For the measured XRD patterns, the change in the integrated intensity of $(0002)_\omega$ and $(222)_\beta$ was evaluated. For $(0002)_\omega$ in the Ti-21V alloy, the peak at $\sim$63.3°, corresponding to the $\{11\bar{2}0\}$ plane in α' phase [23], was excluded from the integration. For the cubic single-crystals after quenching, the independent elastic stiffness components of cubic symmetry, c_{11}, c_{12}, and c_{44}, were measured during aging at temperatures 276–323 K for 10 days. For the c_{ij} measurements, resonant ultrasound spectroscopy [24] combined with electromagnetic acoustic resonance (EMAR) [25] was used. In the RUS analysis, the elastic stiffness components c_{ij} were determined from the resonance vibration frequencies of the specimens, where EMAR was used to identify the vibrational modes of the resonance peaks measured by RUS. The shear modulus $c' = (c_{11} - c_{12})/2$ was calculated using the measured c_{ij} components.

The quenched Ti-21V and Ti-27V alloy single crystals were cooled from 300 to 10 K and were subsequently heated to 300 K. During the cooling and heating experiments, the resonance frequencies f_r and internal friction Q^{-1} of the alloys were measured using EMAR. A free-decay method was used for the measurements of internal friction [26]. In the f_r and Q^{-1} measurements using EMAR, vibration-energy loss and resonance-frequency shift originating from the mechanical contact between a sensor and a specimen are quite small [26], which enable the accurate measurement of f_r and Q^{-1}. For the f_r and Q^{-1} measurements, OY(2) and OX(2) modes were used for the Ti-21V and Ti-27V alloys, respectively. The dimensions of the Ti-21V and Ti-27V alloy specimens, respectively, were $3.739 \times 3.840 \times 3.195$ and $4.338 \times 4.379 \times 3.602$ mm^3. For the heating and cooling experiments, the temperature was changed in steps of 10 or 5 K with an equilibration time of 30 min after every temperature step. The measurement time for the internal friction and resonance frequency at every temperature was approximately 1 h.

Thin foils whose surfaces were parallel to $(110)_\beta$ were cut from the single-crystalline ingots. Subsequently, these foils were subjected to ion milling with 4.0 keV argon ions for perforation. The accelerating voltage for the milling was subsequently decreased to 2.0, 1.0, 0.5, 0.2, and 0.1 kV. Electron diffraction patterns and dark-field images were obtained using transmission electron microscopy (TEM, JEOL JEM-2000EX) operated at 200 kV, whereas atomic-resolution images were obtained using a spherical-aberration-corrected FEI Titan^3 G2 60-300 S/TEM operated at 300 kV. The probe convergence angle and the inner and outer detector angles for high-angle annular dark-field (HAADF) imaging were 17.9 and 50/200 mrad, respectively.

From an arc-melted ingot homogenized at 1273 K for 3 days in vacuum, needle-shaped specimens were prepared using gallium focused-ion-beam (FIB) milling, using an FIB-SEM dual-beam system (FEI, Helios NanoLab600i). A conventional lift-out technique was used for the preparation. Damaged regions near the specimen surface produced via FIB milling were removed using a low-energy Ar ion milling apparatus (Japan Physitec, Gentle Mill IV 5) operated at 0.5 kV. For the prepared specimens, atom probe tomography (APT) measurements were conducted using a local electrode atom probe equipped with a reflection lens (CAMECA, LEAP4000XHR). The measurements were performed in a voltage mode at a specimen temperature of 50 K, and the pulse fraction was 20%. From the measured data, three-dimensional atom maps were reconstructed using a dedicated software program (CAMECA, IVAS-3.6.8). The three-dimensional atom map was divided into a cubic mesh, and the local V concentration c_V in each cube was analyzed. Subsequently, the frequency distribution of c_V in the cubic cells was obtained with the frequency steps of 0.5 at.%. The local c_V analyses were conducted using five different meshing patterns, and the average and standard deviation were evaluated. The length L

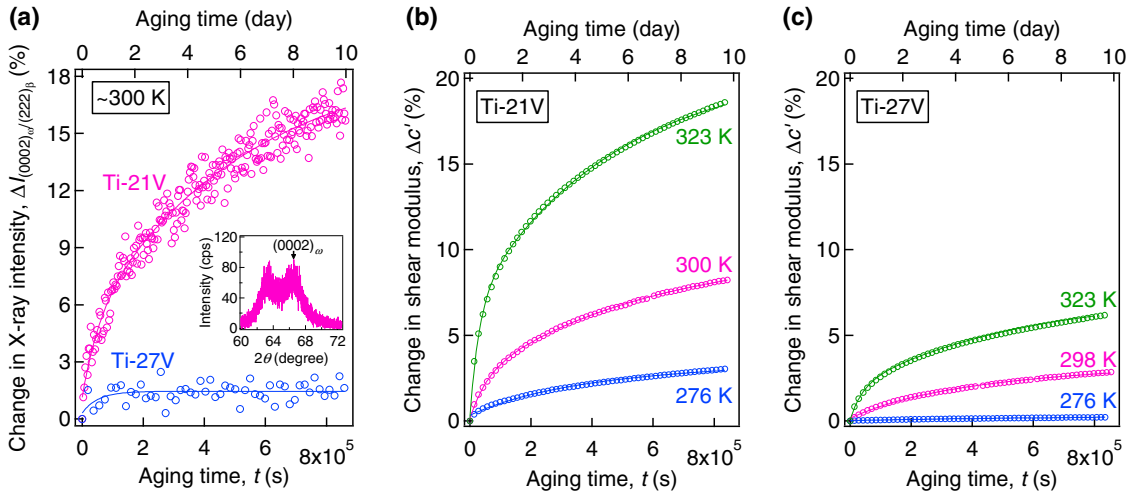

FIG. 1. Formation of ω phase during aging near RT. (a) Change in integrated x-ray intensity of $(0002)_\omega$ in Ti-21V and Ti-27V alloys during aging at ~300 K, where the integrated intensity of $(0002)_\omega$ was normalized by that of $(222)_\beta$. The x-ray diffraction (XRD) patterns near $(0002)_\omega$ after quenching are shown in the inset (Ti-21V) and Fig. S2 in the Supplemental Material [14] (Ti-27V). The peak at ~63.3° corresponds to the $\{11\bar{2}0\}$ reflections of the α' phase [23], and its intensity does not change during aging. The change in shear modulus $\Delta c'$ during aging at 276, ~300, and 323 K is shown in (b) for Ti-21V and in (c) for Ti-27V alloy single crystals. c' is the single-crystalline shear modulus for the $\{110\}_\beta\langle 1\bar{1}0\rangle_\beta$ shear. Even during aging at 323 K for 10 days, the mean V-atom displacement is only 6.4×10^{-5} nm for the Ti-21V alloy and 3.9×10^{-8} nm for the Ti-27V alloy.

of a cubic cell was evaluated based on the detected number of atoms, considering the atomic detection efficiency.

Eshelby's equivalent inclusion method [27,28] was used to evaluate the elastic strain energy $\Delta E_{\rm elas}$ caused by ω-phase nucleation. The nonzero components of the transformation strain (eigenstrain) tensor in the $\beta \rightarrow \omega$ transformation of the Ti-21V alloy are $\epsilon_{11} = \epsilon_{22} = 0.049\%$ and $\epsilon_{33} = 0.427\%$ [23], where the x_1 and x_3 directions are parallel to $[11\bar{2}0]_\omega$ and $[0001]_\omega$, respectively. In the calculation, the elastic stiffness c_{ij} components of the Ti-21V alloy after quenching were used as those of the β-phase matrix, and the c_{ij} components of ω phase were approximated by those of single-crystalline ω phase in pure Ti [29]. The shape of the ω phase particles was assumed as spherical.

III. RESULTS AND DISCUSSION

A. Diffusionless isothermal ω transformation and its driving mechanism

In a Ti-21V alloy [Fig. 1(a)], the normalized $(0002)_\omega$ intensity increases during aging at ~300 K, which indicates that ω phase is formed during aging at RT. Similarly, in the Ti-27V alloy whose β phase is more stable [Fig. 1(a)], ω phase is formed during aging at RT. Notably, in the Ti-21V alloy, ω phase is formed above the athermal ω transformation temperature T_ω of 230 K [22]. In the Ti-27 V alloy, the athermal ω transformation does not occur down to cryogenic temperatures [see Supplemental Material, Fig. S1(b) [14]], but ω phase is formed isothermally at RT.

In the Ti-21V alloy [Fig. 1(b)], the shear modulus c' increases during aging at 276, 300, and 323 K, owing to the formation of ω phase with relatively larger elastic constants [29]. The change in shear modulus $\Delta c'$ increases with the increase in aging temperature, which indicates that the formation of ω phase is accelerated by an increase in the aging temperature. In the Ti-27V alloy [Fig. 1(c)], the shear modulus c' hardly changes at 276 K, which indicates that the formation of ω phase is suppressed by a decrease in temperature. Remarkably, even during aging at 323 K for 10 days, the mean V-atom displacement calculated using its diffusion coefficient [30] is only 6.4×10^{-5} nm for the Ti-21V alloy and 3.9×10^{-8} nm for the Ti-27V alloy. Thus, atomic diffusion could not occur during the present aging processes, but ω phase could be formed isothermally near RT.

The ω phase formed via aging at 323 K for 10 days was observed in the Ti-21V alloy using TEM. Figure 2(a) shows the electron diffraction pattern taken along the $[011]_\beta$ direction. In addition to the diffraction spots from the β phase, diffuse ω phase diffraction spots are observed. In contrast, only diffuse streaks are observed in the alloy after quenching, as shown in the inset of Fig. 2(a). Figure 2(b) shows the TEM dark-field image taken with the ω-phase reflection spot in Fig. 2(a). In the β matrix, a high density of ω phase particles of a few nanometers in size is formed homogeneously. The size and atomic arrangement of the ω phase formed via aging were analyzed using high-angle annular dark-field scanning TEM (HAADF-STEM). Figures 2(c) and 2(d) show the HAADF-STEM image and the overlay of RGB images filtered by using the reflection spots from the ω-phase domains 1 (G: green) and 2 (R: red), respectively. The size of the green and red images in Fig. 2(d) indicates that the size of ω phase particles is limited to a few nanometers. Figure 2(e) shows the magnified and colored HAADF-STEM image of the dashed square region in Fig. 2(c) and the corresponding intensity profiles along the X-Y direction, and Fig. 2(f) shows the atomic arrangement of the β and ω phases. The $\{111\}_\beta$ plane pairs in the central region of the ω phase, indicated by the green square in Fig. 2(e), are almost fully collapsed on

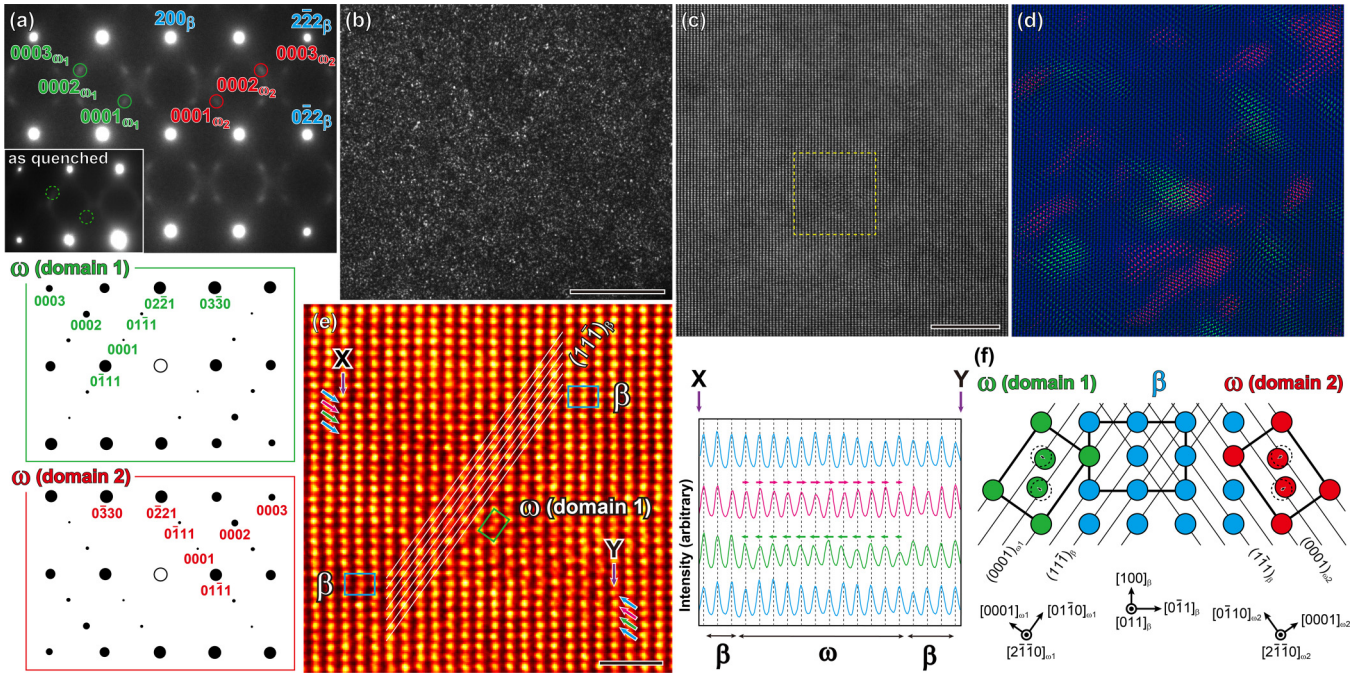

FIG. 2. TEM and HAADF-STEM observations in the Ti-21V alloy after aging at 323 K for 10 days. (a) Electron diffraction pattern taken along the $[011]_\beta$ direction. Calculated electron diffraction patterns for two domains of the ω phase. An electron diffraction pattern of the Ti-21V alloy after quenching is shown in the inset. (b) TEM dark-field image taken with the diffuse reflection spots from the ω phase. Scale bar: 20 nm. (c) HAADF-STEM image taken along the $[011]_\beta$ direction. Scale bar: 5 nm. (d) Overlay of RGB images filtered by using reflection spots from the β phase (B: blue) and domains 1 (G: green) and 2 (R: red) of the ω phase. (e) Magnified and colored HAADF-STEM image of the highlighted region with the dashed square region in (c). Scale bar 1 nm. Intensity profiles along the *X*-*Y* direction. The intensity peaks of the blue profiles are equally spaced in both the β and ω phases while those of the pink and green profiles are shifted towards *Y* and *X*, respectively, in the ω phase as indicated by pink and green arrows. (f) Atomic arrangement of the β phase and two domains of the ω phase viewed along the $[011]_\beta$ direction.

the atomic scale whereas those in the interfacial region of the ω phase are only partially collapsed. This indicates that diffuse ω phase particles can be formed locally on the atomic scale.

Figure 3(a) shows the V atom distribution in cross sections of the Ti-27V alloy after aging at 323 K for 10 days and after aging at 573 K for 1 h, obtained using APT. After aging at 323 K for 10 days, V atoms are homogeneously dispersed. This confirms that solute-atom partitioning via atomic diffusion does not occur during aging at 323 K. In contrast, V-lean regions are formed after aging at 573 K for 1 h, as indicated by the blue arrows. The frequency distribution of local V concentration c_V, shown in Fig. S3 of the Supplemental Material [14], also indicates that V atoms are homogeneously dispersed after aging at 323 K, whereas solute-atom partitioning via atomic diffusion occurs during aging at 573 K. These results show that solute-atom partitioning via atomic diffusion does not occur even during aging at 323 K for 10 days. Accordingly, it is verified that the ω phase is formed via a diffusionless mechanism, i.e., diffusionless isothermal ω transformation occurs near RT. A classification of ω transformations is shown in Fig. 3(f).

According to fluctuation theory in statistical physics [31], the V concentration c_V in the studied Ti-V solid solution fluctuates around its average value in any local region. The probability density of c_V in a region containing N atoms is given by

$$f(c_V) = \frac{1}{\sqrt{2\pi\sigma^2}} \exp\left[-\frac{(c_V - \langle c_V\rangle)^2}{2\sigma^2}\right], \tag{1}$$

with

$$\sigma^2 = \frac{kT}{N(\partial\mu_V/\partial\langle c_V\rangle + \partial\mu_{Ti}/\partial\langle c_{Ti}\rangle)}, \tag{2}$$

where N is the total number of Ti and V atoms in the region that is now considered; σ is the standard deviation of c_V; $\langle c_V\rangle$ and $\langle c_{Ti}\rangle (=1-\langle c_V\rangle)$ are the mean V and Ti concentrations in the alloy, respectively; and μ_V and μ_{Ti} are the chemical potentials of V and Ti, respectively. Equation (2) indicates that the standard deviation σ increases with the decrease in N, i.e., c_V fluctuates largely in a local region containing a small number of atoms.

In the Ti-27V alloy after aging at 323 K for 10 days, the local variation of c_V in cubic cells was analyzed using APT. Figure 3(b) shows the relative frequency of c_V in cubic cells with the length $L = 3.5$ nm. The plots denote the APT measurements and the line denotes the relative frequency evaluated using a binominal distribution, which corresponds to the frequency distribution in the ideal solution of the Ti-27V alloy [see Supplemental Material, Figs. S4(a) and S4(b) and their explanations [14]]. In an ideal solution, the standard deviation σ in Eq. (2) is simply reduced to $\sigma = \sqrt{\langle c_V\rangle(1-\langle c_V\rangle)/N}$

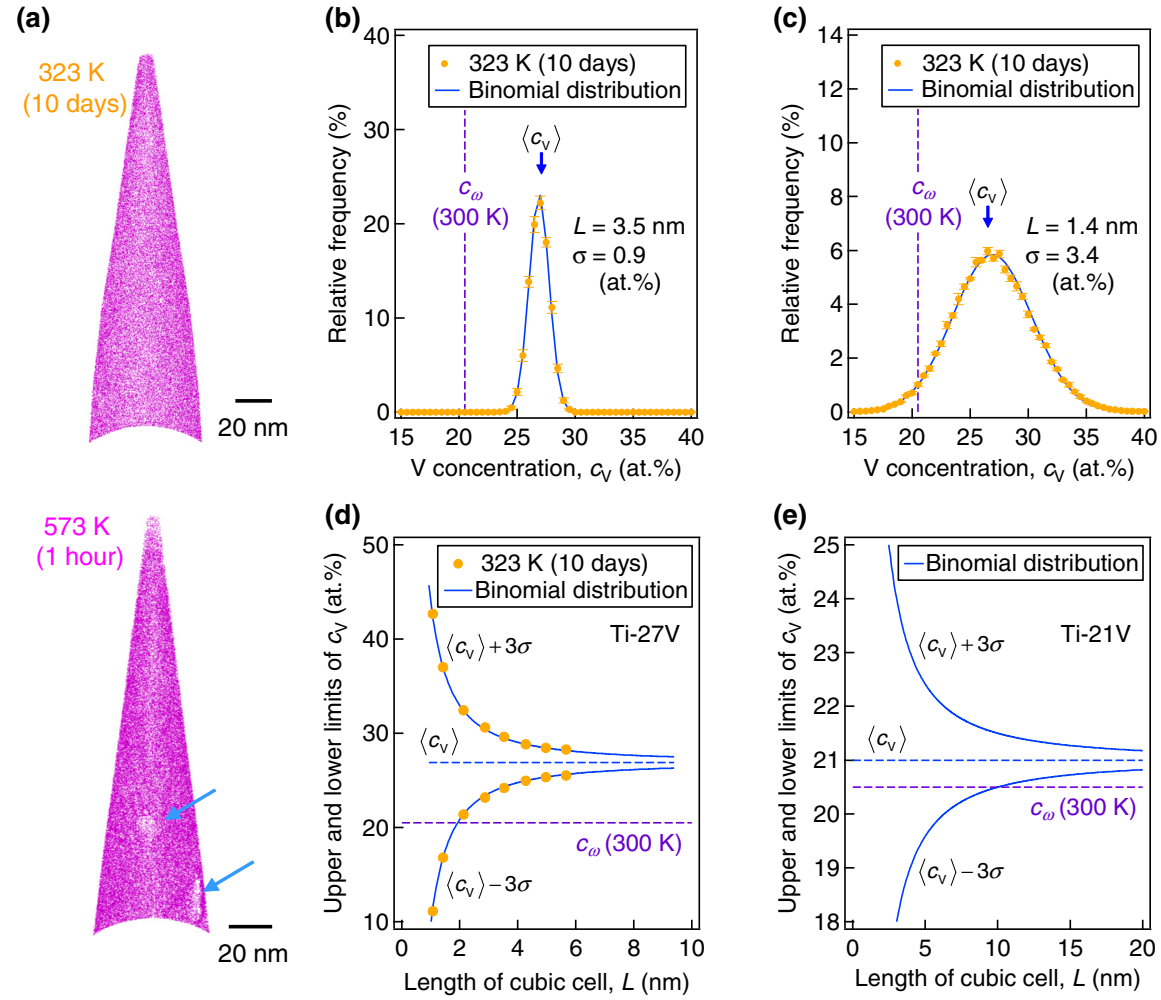

(f)

	Long incubation time	Short incubation time
With diffusion	Diffusion-mediated isothermal ω transformation	
Without diffusion	**Diffusionless isothermal ω transformation**	Diffusionless athermal ω transformation

FIG. 3. APT analyses of the V-atom distribution. (a) V-atom distributions in cross sections of the Ti-27V alloy after aging at 323 K for 10 days and after aging at 573 K for 1 h, obtained using APT. The relative frequency of V concentration c_V in cubic cells with length L, in the Ti-27V alloy after aging at 323 K for 10 days: $L = 1.4$ (b) and 3.5 nm (c). The error bars denote the standard deviation from five rounds of APT analyses. In (d) Ti-27V and (e) Ti-21V alloys, the upper and lower limits of V concentration, $\langle c_V \rangle + 3\sigma$ and $\langle c_V \rangle - 3\sigma$, in cubic cells with length L are shown. The blue dashed lines indicate the macroscopic average of V concentration $\langle c_V \rangle$, and the purple dashed lines denote c_ω that is the V concentration where athermal ω transformation occurs at 300 K. (f) Classification of ω transformations.

(binominal distribution), with $N = nL^3$, where n is the number density of atoms in the cell. For $L = 3.5$ nm [Fig. 3(b)], being sufficiently large compared to the positional resolution ($\sim 1 \times 1 \times 0.2$ nm^3) of the present APT apparatus, the measured V concentration c_V fluctuates around the macroscopic average $\langle c_V \rangle$. However, all the measured c_V values are larger than c_ω (the purple dashed line) that is the V concentration where the athermal ω transformation occurs at 300 K. In Fig. 3(b) the frequency distribution of the measured c_V is almost the same as that evaluated using a binominal distribution, i.e., the measured frequency distribution is almost equal to that in the ideal solution [see Supplemental Material, Figs. S4(a) and S4(b) and their explanations [14]]. On the other hand, when L is set at 1.4 nm [Fig. 3(c)], c_V fluctuates strongly. Consequently, it deserves to note that, at this length scale, there exist the relative frequencies corresponding to the V concentration below c_ω (300 K).

Here we discuss a mechanism of the diffusionless isothermal ω transformation. Figure 3(d) shows the variation of V concentration c_V as a function of the cell length L. The plots are the $\langle c_V \rangle + 3\sigma$ and $\langle c_V \rangle - 3\sigma$ values obtained from the APT measurements, and the lines denote the same values evaluated using binominal distributions. The V concentration c_V fluctuates within the range between $\langle c_V \rangle - 3\sigma$ and $\langle c_V \rangle + 3\sigma$ with a probability of 99.7%, whereas it fluctuates within the range between $\langle c_V \rangle - 2\sigma$ and $\langle c_V \rangle + 2\sigma$ with a probability of 95.4%. The range expressed by the $\langle c_V \rangle \pm 3\sigma$ values covers the fluctuated V concentrations almost entirely,

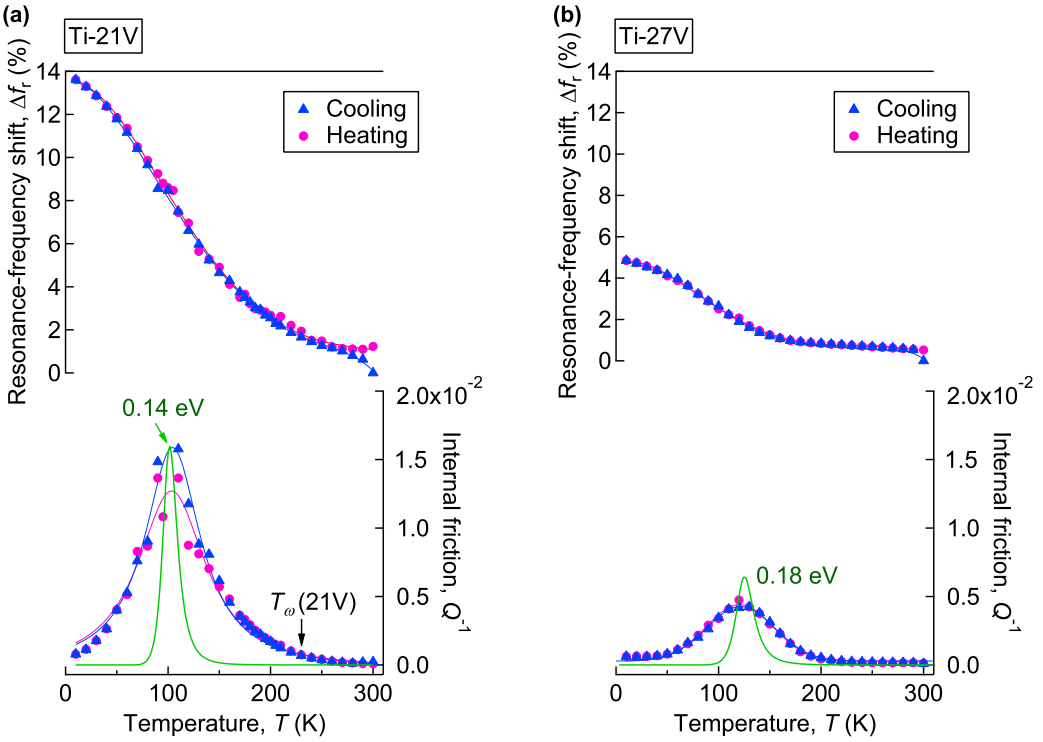

FIG. 4. Temperature dependence of resonance frequency and internal friction. Change in resonance frequency Δf_r and internal friction Q^{-1} in (a) Ti-21V and (b) Ti-27V single crystals after quenching, upon cooling and heating. The resonance frequency values at 300 K after quenching the Ti-21V and Ti-27V alloys are 513.592 and 456.512 kHz, respectively. The green lines are the Debye-function fits.

even though the $\langle c_V \rangle \pm 2\sigma$ values can also express the range of the fluctuated V concentrations with a high probability. Therefore, $\langle c_V \rangle + 3\sigma$ and $\langle c_V \rangle - 3\sigma$ are referred to as the upper and lower limits of c_V, respectively, and their values are used for the discussion of the fluctuated V concentrations. In both the measurements and binominal distributions [Fig. 3(d)], the upper limit $\langle c_V \rangle + 3\sigma$ increases and the lower limit $\langle c_V \rangle - 3\sigma$ decreases with the decrease in L. In regions of $L < \sim 2$ nm [Fig. 3(d)], the lower limit $\langle c_V \rangle - 3\sigma$ is smaller than c_ω(300 K). In such local V-lean regions of a few cubic nanometers in size, ω transformation can occur at 300 K. In contrast, in larger volumes, the fluctuation is small, i.e., c_V is close to the average $\langle c_V \rangle$. Thus, large ω particles cannot be formed. This is confirmed by the fact that athermal ω transformation, which forms large ω particles, does not occur at RT in the Ti-27V alloy. Figure 3(e) shows the upper and lower concentration limits of c_V in the Ti-21V alloy, evaluated using binominal distributions. For $L < \sim 9$ nm, the lower limit $\langle c_V \rangle - 3\sigma$ is smaller than c_ω (300 K). Thus, ω transformation can occur in the local V-lean regions of $L < \sim 9$ nm. This is confirmed by the HAADF-STEM observation, which shows that the size of ω phase particles formed during aging near RT is limited to a few nanometers.

The presented statistical analyses show that, in V-lean regions, which are inevitably present owing to quenched-in compositional fluctuations, the ω phase can be formed locally even if the β-phase region is stable on average. This explains how diffusionless isothermal ω transformation can occur even in highly stabilized alloys where athermal ω-transformation cannot occur. Furthermore, quenched-in compositional fluctuations also explain how the diffuse ω structure (localized ω phase) is formed above T_ω and why athermal ω transformation cannot occur in the entire matrix at T_ω [see Supplemental Material, Fig. S4(c) and its explanation [14]].

B. Kinetic process of time-dependent diffusionless isothermal ω transformation

Figure 4(a) shows the change in the acoustic resonance frequency Δf_r and internal friction Q^{-1} during the cooling and heating processes in the Ti-21V alloy. The internal friction Q^{-1} was measured at temperatures higher and significantly lower than $T_\omega(21V) = 230$ K. The broad Q^{-1} peak appears at $\sim$100 K, which is significantly lower than T_ω. In terms of the resonance frequency, f_r steeply increases below 150 K, where Δf_r is approximately proportional to $\sqrt{\Delta c'}$ [see Supplemental Material, Fig. S5(a) [14]]. This increase in f_r is attributed to the ΔM effect [32] related to the Q^{-1} peak [see Supplemental Material, Fig. S5(c) [14]]. Moreover, the increase in f_r is caused by the athermal ω transformation occurring below T_ω. Above $\sim$280 K, the resonance frequency f_r upon heating becomes larger than that upon cooling, which is caused by the diffusionless isothermal ω transformation during the measurement process [see Supplemental Material, Fig. S6(a) [14]]. In the Ti-27V alloy [Fig. 4(b)], the resonance frequency f_r upon the heating and cooling processes changes strongly below 170 K, owing to the ΔM-effect. The Q^{-1} peak appears at $\sim$120 K, where neither the diffusionless isothermal nor athermal transformation occurs [see Fig. 1(c) and Fig. S6(b) in the Supplemental Material [14]].

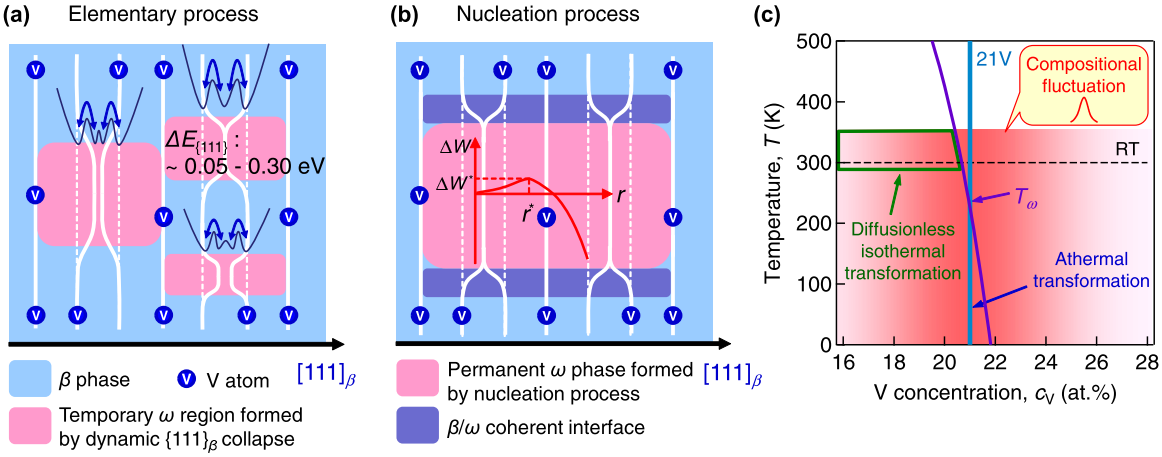

FIG. 5. Kinetics of diffusionless isothermal and athermal ω transformations. (a) Schematic illustration showing temporary ω regions formed by the dynamic $\{111\}_\beta$ collapse. The temporary ω region is not a permanent ω phase, as the precipitate cannot reach the critical size necessary to compensate for the energy gain caused by the β/ω coherent phase boundary. (b) Schematic illustration showing a permanent ω phase formed by a nucleation process with the β/ω coherent interface. (c) Schematic illustration explaining the effect of compositional fluctuations on diffusionless isothermal and athermal ω transformations in the Ti-21V alloy.

Sommer *et al.* [33,34] suggested that the anelastic relaxation causing Q^{-1} is the dynamically fluctuated $\{111\}_\beta$ collapse ("dynamic $\{111\}_\beta$ collapse"), which occurs in local β regions where ω transformation has not occurred yet. The temperature of a Q^{-1} peak depends on the frequency f_r used for the Q^{-1} measurement and obeys the Debye relaxation function [33,34], which indicates that the dynamic $\{111\}_\beta$ collapse can occur at various temperatures even where the ω transformation does not occur (see Supplemental Material, Supplemental Note 1 [14]). Therefore, we regard the dynamic $\{111\}_\beta$ collapse as the elementary process of the ω transformation, which forms a temporary ω structure and does not necessarily result in the ω transformation, i.e., the ω-phase nucleation. The temporary ω structure formed by the dynamic $\{111\}_\beta$ collapse is schematically illustrated in Fig. 5(a). Notably, owing to the compositional fluctuations, the less stable β regions, where dynamic $\{111\}_\beta$ collapse occurs, are possibly present at various temperatures where the β phase is retained. As shown in Figs. S5(d) and S6(b) of the Supplemental Material [14], Q^{-1} decreases via diffusionless ω isothermal transformation, which confirms that the dynamic $\{111\}_\beta$ collapse causing Q^{-1} occurs in less stable β-phase regions, formed by the compositional fluctuation.

The dynamic $\{111\}_\beta$ collapse is the elementary process of the transformation. Thus, an ω-phase nucleation process is additionally required for the occurrence of the ω transformation, as schematically illustrated in Fig. 5(b). Accordingly, we propose that the ω-transformation rate I is given by the combination of the frequency of the dynamic $\{111\}_\beta$ collapse forming a temporary ω structure and the probability of the nucleation forming a permanent ω phase:

$$I \propto f_0 \exp(-\Delta E_{\{111\}}/kT)\exp(-\Delta W^*/kT), \qquad (3)$$

where f_0 is the frequency factor of the dynamic $\{111\}_\beta$ collapse, and $\Delta E_{\{111\}}$ and ΔW^* are the activation energies of the dynamic $\{111\}_\beta$ collapse and the ω-phase nucleation, respectively (see Supplemental Material, Supplemental Note 2 [14]).

The energy barrier for the dynamic collapse originates from the free energy barrier between the β and ω structures. Here the free energy is a function of the degree of the $\{111\}_\beta$ collapse which can express the transient state between the β and ω structures. The dynamic $\{111\}_\beta$ collapse occurs locally in less stable β-phase regions. Thus, the distortion of $(0002)_\omega$ and $(111)_\beta$ occurs during the activation process [Fig. 5(a)], which causes the interface energy between the β structure and the transition state. In the ω transformation, the elastic strain energy caused by the transformation strain is low as explained later. Thus, the elastic strain energy is probably low during the activation process. Therefore, the energy barrier for the dynamic $\{111\}_\beta$ collapse mainly originates from the free energy barrier between the β and ω structures and the interface energy between the β structure and the transition state.

The activation energy $\Delta E_{\{111\}}$ of the dynamic $\{111\}_\beta$ collapse in Eq. (3) was evaluated by analyzing the $Q^{-1}(T)$ curve of the Ti-21V alloy [Fig. 4(a)], using the Debye function [32]:

$$Q^{-1} = \Delta \frac{\omega_r \tau_0 \exp(\Delta E_{\{111\}}/kT)}{1 + [\omega_r \tau_0 \exp(\Delta E_{\{111\}}/kT)]^2}, \qquad (4)$$

where Δ is the relaxation strength, $\omega_r(=2\pi f_r)$ is the angular frequency, $\tau_0(=1/f_0)$ is the time constant $(2.2 \times 10^{-14}$ s) [33], and k is the Boltzmann constant. The analysis revealed that the activation energy $\Delta E_{\{111\}}$ corresponding to the peak is as small as 0.14 eV. In Fig. 4(a) the measured Q^{-1} peak is broader than the Debye-function fit denoted by the green line, which indicates that $\Delta E_{\{111\}}$ takes multiple values. More detailed analyses, shown in Fig. S7(a) of the Supplemental Material [14], revealed that the $\Delta E_{\{111\}}$ values are widely distributed in the range ~0.05–0.30 eV. In the Ti-27V alloy [Fig. 4(b)], the activation energy $\Delta E_{\{111\}}$ for the peak is 0.18 eV, which is higher than that in the Ti-21V alloy. This indicates that the activation energy increases with the increase in β-phase stability. In the Ti-27V alloy, the $\Delta E_{\{111\}}$ values are also widely distributed in the range ~0.05–0.25 eV [see Supplemental Material, Fig. S7(b) [14]]. These large variations

of the activation energy are probably attributed to the spatial distribution of β-phase stability, formed by the compositional fluctuations.

For a spherical ω nucleus with a radius r, the activation energy of nucleation in Eq. (3) is given by $\Delta W^* = 16\pi\gamma^3/[3(\Delta G_{\omega-\beta} + \Delta E_{\rm elas})^2]$, where γ is the β/ω coherent interface energy, $\Delta G_{\omega-\beta}$ is the chemical free energy difference between ω and β phases, and $\Delta E_{\rm elas}$ is the elastic strain energy caused by the transformation strain (eigenstrain). In the ω transformation, the transformation strain is small [23]. Thus, the elastic strain energy caused by the transformation strain is low; $\Delta E_{\rm elas} = 0.716\,{\rm MJ}\cdot{\rm m}^{-3}$. Therefore, the elastic strain energy can be compensated by the small undercooling (ΔT) of ~ -1 K, where $\Delta G_{\omega-\beta} = 0.647\Delta T$ MJ $\cdot$ m^{-3} [35]. Consequently, ΔW^* mainly depends on the chemical free energy difference $\Delta G_{\omega-\beta}$ and the β/ω interface energy. Here the β/ω interface energy γ mainly originates from the elastic energy caused by the distortion of $(111)_\beta$ and $(0002)_\omega$ around the β/ω coherent interface [Fig. 5(b)]. Thus, γ depends on the degree of $2/3[111]_\beta$-phonon softening, and the phonon softening leads to a low γ value.

In the diffusionless isothermal transformation near RT [Fig. 5(c)], ω phase particles nucleate in local V-lean regions, by utilizing local free energy differences $\Delta G_{\omega-\beta}$ formed by compositional fluctuations. The local V-lean regions are inevitably surrounded by stable β regions in which $2/3[111]_\beta$-phonon softening is less pronounced. Owing to this localized $2/3[111]_\beta$-phonon softening, a high elastic energy is required for the distortion of $(0002)_\omega$ and $(111)_\beta$, and thus, the β/ω interface energy is high. Consequently, ΔW^* of the nucleation process is high, and thus, the probability of nucleation $\exp(-\Delta W^*/kT)$ is low. Therefore, diffusionless ω transformation occurs at slow transformation rates, even though the elementary process corresponding to the dynamic $\{111\}_\beta$ collapse is frequent ($\sim$200 GHz) at RT, as shown in Fig. S7(c) of the Supplemental Material [14]. Owing to the high ΔW^* of the nucleation process, diffusionless isothermal transformation is suppressed at low temperatures, and thus, it occurs only near and above RT. Notably, the small transformation strain is important for an ω phase to nucleate by utilizing a local-negative $\Delta G_{\omega-\beta}$ formed by the compositional fluctuations, because the corresponding low elastic strain energy $\Delta E_{\rm elas}$ can easily be compensated by the local-negative $\Delta G_{\omega-\beta}$. Thus, in the ω transformation, the localized phonon softening, which occurs in locally unstable regions, can lead to the transformation, being "uncooperative" with other stable regions. This mechanism of the localized transformation is distinct from that of displacive transformations with large transformation strains, which "cooperatively" occur in widely spread regions, accompanied by the softening of long wavelength acoustic phonon at the gamma point.

Below the athermal ω transformation temperature T_ω, most of the β region is unstable, as shown in Fig. 5(c). Thus, $2/3[111]_\beta$-phonon softening occurs in most of the β matrix, and therefore, ω nuclei are surrounded by unstable β regions. Consequently, the β/ω interface energy γ around the nucleus is negligible, as in the case of the nucleation near the instability temperature of the first-order transformation. In this case, ΔW^* of the nucleation process is low. Therefore, athermal ω transformation occurs instantaneously even at low temperatures, because the dynamic $\{111\}_\beta$ collapse is still frequent at low temperature ($\sim$14 GHz at 200 K), as shown in Fig. S7(c) of the Supplemental Material [14]. Accordingly, the transformation rates of both diffusionless isothermal and athermal ω transformations are dominated by the two activation processes: the dynamic $\{111\}_\beta$ collapse and nucleation process. However, their transformation rates are different, originating from the difference in the nucleation probabilities reflecting the β/ω interface energy, that is, the nucleation probability is the rate-determining process in the ω transformation. The β/ω interface energy depends on the spatial distribution of unstable β regions formed by compositional fluctuations. Thus, the compositional fluctuations dominate the kinetics of ω transformation as well as the thermodynamics of the transformation.

IV. CONCLUSIONS

We revealed that diffusionless isothermal ω transformation occurs in local V-lean regions formed by quenched-in compositional fluctuations even when athermal ω transformation cannot occur. This anomalous, localized transformation originates from the localized softening of $2/3[111]_\beta$ longitudinal phonon, which occurs in unstable V-lean regions formed by the quenched-in compositional fluctuations. Therefore, the localized transformation cannot be suppressed by the stabilization of β phase on average. The transformation rates of both diffusionless isothermal and athermal ω transformation are dominated by the frequency of the dynamic $\{111\}_\beta$ collapse and the probability of ω-phase nucleation, but the activation energy of the nucleation process results in an evident difference in their transformation rates. The quenched-in compositional fluctuations determine the activation energies of the nucleation process and the dynamic $\{111\}_\beta$ collapse, and thus, the compositional fluctuation is the key factor to understand the thermodynamics and kinetics of ω transformation.

ACKNOWLEDGMENTS

This work was supported by JSPS KAKENHI Grants No. 26709053 and No. 17H03414, and research grants from the Light Metal Educational Foundation, Amada Foundation, and Kansai Research Foundation for technology promotion.

[1] T. Saito *et al.*, Science **300**, 464 (2003).
[2] D. Banerjee and J. C. Williams, Acta Mater. **61**, 844 (2013).
[3] M. Long and H. J. Rack, Biomaterials **19**, 1621 (1998).
[4] H. Y. Kim, Y. Ikehara, J. I. Kim, H. Hosoda, and S. Miyazaki, Acta Mater. **54**, 2419 (2006).
[5] J. Zhang, C. C. Tasan, M. J. Lai, A. C. Dippel, and D. Raabe, Nat. Commun. **8**, 14210 (2017).
[6] A. Devaraj, V. V. Joshi, A. Srivastava, S. Manandhar, V. Moxson, V. A. Duz, and C. Lavender, Nat. Commun. **7**, 11176 (2016).

[7] M. Bönisch, A. Panigrahi, M. Stoica, M. Calin, E. Ahrens, M. Zehetbauer, W. Skrotzki, and J. Eckert, Nat. Commun. **8**, 1429 (2017).

[8] S. K. Sikka, Y. K. Vohra, and R. Chidambaram, Prog. Mater. Sci. **27**, 245 (1982).

[9] M. Tane, T. Nakano, S. Kuramoto, M. Hara, M. Niinomi, N. Takesue, T. Yano, and H. Nakajima, Acta Mater. **59**, 6975 (2011).

[10] D. de Fontaine, N. E. Paton, and J. C. Williams, Acta Metall. **19**, 1153 (1971).

[11] S. Nag *et al.*, Phys. Rev. Lett. **106**, 245701 (2011).

[12] M. J. Lai, C. C. Tasan, J. Zhang, B. Grabowski, L. F. Huang, and D. Raabe, Acta Mater. **92**, 55 (2015).

[13] D. Choudhuri *et al.*, Acta Mater. **130**, 215 (2017).

[14] See Supplemental Material at http://link.aps.org/supplemental/10.1103/PhysRevMaterials.3.043604 for Figs. S1–S7 and Supplemental Notes 1 and 2.

[15] A. Planes, E. Obradó, A. Gonzàlez-Comas, and L. Mañosa, Phys. Rev. Lett. **79**, 3926 (1997).

[16] S. Singh *et al.*, Nat. Commun. **8**, 1006 (2017).

[17] W. Petry, A. Heiming, J. Trampenau, M. Alba, C. Herzig, H. R. Schober, and G. Vogl, Phys. Rev. B **43**, 10933 (1991).

[18] C. B. Walker, Phys. Rev. B **28**, 674 (1983).

[19] Z. Fan, Scr. Metall. Mater. **31**, 1519 (1994).

[20] Y. Al-Zain, Y. Sato, H. Y. Kim, H. Hosoda, T. H. Nam, and S. Miyazaki, Acta Mater. **60**, 2437 (2012).

[21] M. Tane, K. Hagihara, M. Ueda, T. Nakano, and Y. Okuda, Acta Mater. **102**, 373 (2016).

[22] N. E. Paton and J. C. Williams, Scr. Metall. **7**, 647 (1973).

[23] G. Aurelio, A. Fernández Guillermet, G. J. Cuello, and J. Campo, Metall. Mater. Trans. A **33**, 1307 (2002).

[24] I. Ohno, J. Phys. Earth **24**, 355 (1976).

[25] H. Ogi, H. Ledbetter, S. Kim, and M. Hirao, J. Acoust. Soc. Am. **106**, 660 (1999).

[26] M. Hirao and H. Ogi, *EMATs for Science and Industry: Noncontacting Ultrasonic Measurements* (Kluwer Academic Publishers, Dordrecht, 2013).

[27] J. D. Eshelby, Proc. Royal Soc. London A **241**, 376 (1957).

[28] T. Mura, *Micromechanics of Defects in Solids*, 2nd rev. ed. (Kluwer Academic Publishers, Dordrecht, 1987)

[29] M. Tane, Y. Okuda, Y. Todaka, H. Ogi, and A. Nagakubo, Acta Mater. **61**, 7543 (2013).

[30] H. Nakajima and M. Koiwa, ISIJ Int. **31**, 757 (1991).

[31] L. Landau and E. Lifshitz, *Statistical Physics: Vol. 5: Course of Theoretical Physics* (Pergamon Press, Oxford, 1968).

[32] A. Nowick and B. Berry, *Anelastic Relaxation in Crystalline Solids* (Academic Press, New York, 1972).

[33] A. W. Sommer, S. Motokura, K. Ono, and O. Buck, Acta Metall. **21**, 489 (1973).

[34] C. W. Nelson, D. F. Gibbons, and R. F. Hehemann, J. Appl. Phys. **37**, 4677 (1966).

[35] J. Y. Yan and G. B. Olson, J. Alloys Compd. **673**, 441 (2016).